Effectiveness of a TRM solution for rammed earth under in-plane cyclic loads

Romanazzi A.[1], Oliveira D.V.[2], Silva R.A.[3] and Barontini A.[4]

1. ISISE, Department of Civil Engineering, University of Minho, Guimarães, Portugal, aromanazzi89@gmail.com, https://orcid.org/0000-0003-1684-8826
2. ISISE, Department of Civil Engineering, University of Minho, Guimarães, Portugal, danvco@civil.uminho.pt, https://orcid.org/0000-0002-8547-3805
3. ISISE, Department of Civil Engineering, University of Minho, Guimarães, Portugal, ruisilva@civil.uminho.pt, https://orcid.org/0000-0002-1115-107X
4. ISISE, Department of Civil Engineering, University of Minho, Guimarães, Portugal, albe.barontini@gmail.com, https://orcid.org/0000-0001-8377-8149

Abstract

To evaluate the effectiveness of a TRM-strengthening solution for rammed earth walls subjected to in-plane cyclic loads, an experimental program was conducted on a strengthened mock-up previously damaged. The experimental results are discussed in comparison with the previous unstrengthened model in terms of cracking pattern, damage identification, displacements, base shear coefficient, stiffness degradation, and energy dissipation; in addition, simplified equivalent linear and bi-linear systems are inferred to assess the performance. The outcomes highlighted the effectiveness of the TRM solution in improving the in-plane shear capacity, the ductility and the dissipated energy of the mock-up.

Keywords: compatible textile reinforced mortar, rammed earth, in-plane cyclic loading, energy-based analysis, dynamic identification, stiffness degradation, seismic capacity.

1 Introduction

Earthen materials have been widely used by different human civilizations in vernacular technique becoming part of architectural heritage which must be preserved [1][2]. The low mechanical properties of the material, lack of maintenance practices, and deficiencies in the building process result in high seismic vulnerability of earthen architecture, which leads to in-plane cracking or out-of-plane collapse mechanisms of the bearing walls under intense earthquakes [3][4][5][6]. The concern about mitigating the seismic vulnerability of existing rammed earth buildings further increased when their high seismic risk turned into calamities[7][8][9]. However, the former lack of scientific and technological knowledge is evident when techniques and approaches commonly used for other structural systems were adapted for earthen building without any critical analysis, causing further degradation or increasing the seismic vulnerability [9][10]. In this context, the requirement of "compatibility" of the solution must be considered, which intends to ensure that the introduced treatment materials will not induce negative consequences, guaranteeing the long-term effectiveness of the intervention [11].

With regard to strengthening solutions for existing earthen structures, adobe masonry scaled mock-ups strengthened with an externally embracing timber or steel system were already tested. In this way, the formation of out-of-plane collapse mechanisms was limited, and the in-plane structural ductility was increased [4][12][13][14][15]. Despite the above-described systems provide a general improvement of the in-plane and out-of-plane capacity of the earth walls, such solutions might be invasive or not compatible with the existing buildings. A further strengthening technique based on textile-reinforced mortar (TRM) has been developed in the last decades [16][17][18], in particular for masonry buildings, and it was demonstrated to be efficient to mitigate the vulnerability of masonry structures due to its great tensile strength and reduced self-weight [19][20]. The investigation of TRM as a strengthening solution for earthen buildings was widely addressed by the Pontificia Universidad Católica del Peru (PUCP), in response to high the seismic risk associated with the Peruvian adobe housing [4][21][22][23][24][25][26][27][28]. The outcomes demonstrate an improvement of the in-plane capacity and overall structural ductility; while, the out-of-plane overturning of the adobe walls was prevented, despite the evident damaged [27][29][30][31]. In [28][32][33][34], different types of meshes (geosynthetic, plastic or metallic meshes) strengthening walls of adobe dwellings were tested and showed an improvement of the seismic capacity of the structure, in particular when geosynthetic meshes are applied. Similar results with the use of a synthetic mesh were achieved in [27]. In [29], cyclic in-plane tests were performed on an adobe wall, which was repaired and then strengthened with plastic mesh. It was observed that the stiffness of the adobe wall could be recovered with a significant improvement of the ductility, energy dissipation, and shear capacity, while preventing the fragile failure. The first outcomes on the application of externally bonded fibres for rammed earth walls report an improvement of the overall seismic capacity similar to that attained for adobe masonry [8][35][36][37][38]. In [39], near surface mounted polyester fabric strips applied on rammed earth walls with cement mortar increased the in-plane energy dissipation and the ductility. Satisfactory improvement of the in-plane capacity of rammed earth walls strengthened with tarpaulin strips bonded externally with an inorganic compound is reported in [40]. In [34], it was found that steel welded meshes can improve the in-plane shear strength and the out-of-plane capacity of rammed earth wall by preventing premature local failures and by providing confinement after cracking.

However, the use of externally bonded textiles to increase the lateral load capacity and ductility of a rammed earth walls is rather recent, while a lack of investigation on the effectiveness of rammed earth walls strengthened with a TRM solution and subjected to in-plane cyclic loads has been observed in literature. Whitin this framework, an experimental program was undertaken to assess the performance of a rammed earth sub-assembly strengthened with TRM. In particular, the proposed solution is composed of a geomesh embedded in earth-based mortar and anchored with common plastic connectors. It is also reported that the present work is a progression of a previous investigation on the in-plane cyclic performance of an unstrengthened rammed earth wall [41], hereinafter referred to as URE-IP; in this way, the effectiveness of the TRM solution on a damaged structure was evaluated. This paper presents at first the test setup and the applied TRM-strengthening solution; namely, the materials used for the TRM, the strengthening scheme and the fixing system are illustrated. Afterwards, the experimental results are reported in terms of cracking pattern, dynamic characterisation, displacement capacity, base shear forces and strength decay. Further discussion is addressed on the stiffness degradation and energy dissipation, which allowed determining the equivalent damping coefficient. Subsequently, equivalent elastic and elastic-perfectly plastic systems were proposed based on the experimental curves, according to simplified models for masonry structures [42][43][44][45].

2 Experimental program

2.1 Strengthening of the damaged model

The tested mock-up represents a rammed earth structural wall component from a traditional single-storey building with timber roof and I-shape geometry in plan, which allowed to investigate the in-plane performance of a rammed earth wall. It was built with two wing-walls with 120 cm length and a web-wall with 280 cm length, with a thickness of 40 cm and the height of 180 cm (Fig. 1). The rammed earth wall was built by mechanical compaction of an earth moistened mixture in layers of about 10 cm thick using a complete timber mould; as well, to simulate the stress state imposed by a typical timber roof, a total load of 11.77 kN was added on top as mortar bags. The rammed earth mixture was composed of 6% of clay, 9% of silt, 38% of sand and 47% of gravel, and the optimal water content was assessed by means of standard Proctor test [46], resulting in 12% to attain a dry density of 2.02 g/cm^3. In addition, the mechanical characterization of the rammed earth material was performed, resulting in a compressive strength, f_c, of 0.56 MPa, and Young's modulus, E, of 213 MPa. Further details can be found in [41].

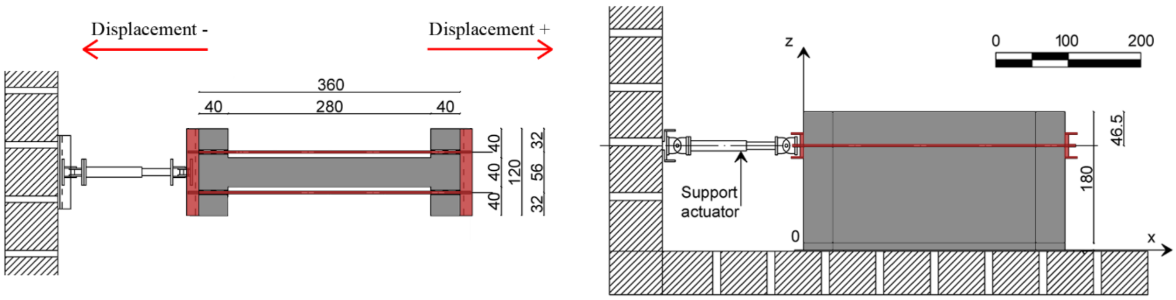

(a) (b)

Fig. 1 GeoRE-IP mock-up geometry: a) plan view, and b) elevation view.

The rammed earth wall was previously tested and damaged [41], and then was strengthened with a compatible TRM solution with the use of geomesh (GeoM), which was embedded in a layer of earth-based mortar of about 10 mm thick. The TRM-strengthened model is hereinafter referred to as GeoRE-IP. The GeoM presented a net aperture of 22X25 mm^2 (Fig. 2a) and woven union between the yarns (Fig. 2b), which were composed of bonded filament with a cross section of 3.09 mm^2 (Fig. 2c and Fig. 2d). Being the features of the mesh different along the orthogonal orientations, the linear density (TEX) [47] was calculated for both the longitudinal (X) and transversal (Y) directions separately, resulting $TEX_{\mathrm{X}} = 4210$ g/km and $TEX_{\mathrm{Y}} = 2820$ g/km; while grammage (GSM) [48] referred to the entire mesh was 215 g/cm^3. Therefore, according to [49], the GeoM meets the grammage requirement for fabrics integrating composites materials, whose value should be lower than 600 $\mathrm{g/m^2}$. The tensile behaviour of the dry meshes was evaluated according to [50] and [51]. The average peak load resulted in 42.08 $\mathrm{kN/m}$ (CoV = 3%) with an elongation of 0.097 $\mathrm{mm/mm}$ (CoV = 3%). The tensile strength (f_t) was assessed considering the maximum force evenly distributed through the number of effective yarns and the cross section of the threads. Accordingly, the resulting average f_t was 340.46 MPa (CoV = 3%). The Young's modulus (E_y) was calculated through a linear regression of the stress-strain values in the range 0-30% of f_t obtaining 2626 MPa (CoV = 6%).

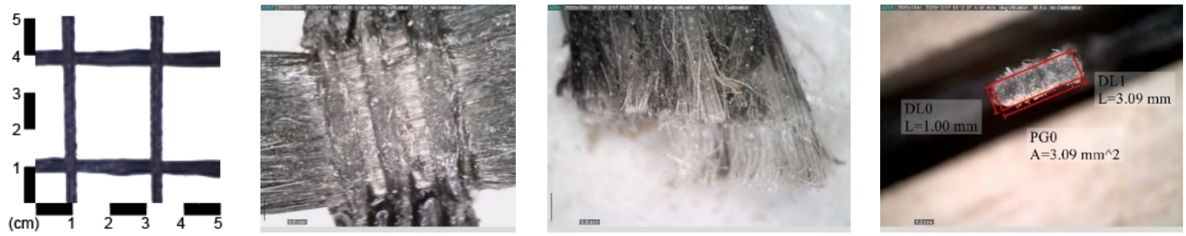

(a) (b) (c) (d)

Fig. 2 Geomesh selected for the experimental program: a) geometry, b) intersection, c) detail of the section, and d) cross section dimension.

Additionally, to guarantee the compatibility between the rammed earth wall and the strengthening solution, the raw soil used to build the model was considered to design the earth-based mortar. Therefore, the raw soil was previously sieved through sieve #10 (2 mm) to remove large particles, thereof sand was added to reduce the clay content to 6% to mitigate shrinkage. Thus, the water content (W/S) for the optimal workability was iteratively defined as 20%, according to the flow table test (Fig. 3a) [52] and by setting a value of 170 mm, as suggested in [53]. Afterwards, the mechanical properties were defined according to EN 1015-11 [54] (Fig. 3b and Fig. 3c). The compressive strength (f_c) resulted 0.49 MPa (CoV = 3%), while the flexural strength (f_b) was 0.21 MPa (CoV = 5%), which are found to be consistent with the values of earth-based mortars found in the literature [53][55]. Subsequently, the Young's modulus was evaluated by means of axial compression tests on three cylindrical specimens with 90 mm of diameter and 175 mm of height (Fig. 3d), which resulted in 1232 MPa (CoV = 14%).

(a) (b) (c) (d)

Fig. 3 Characterisation of the earth-based mortar: a) flow table test, b) three-point bending test, c) compression test, and d) Young's modulus.

Before applying the mortar, the surface of the web-wall was scraped and wet, in order to favour the adherence of the mortar to the substrate and avoid early water suction, and consequent shrinkage. The scheme of TRM-strengthening is reported in Fig. 4 and Fig. 5. Since the main crack had a dominant horizontal orientation, mesh bands with 1000 mm width were applied with a rotation of 16º (with respect to the horizontal direction) to optimize the strengthening capacity with respect to damage pattern resulting from the URE-IP test. To guarantee an even distribution of the loads during the cyclic actions, two mesh bands were applied on each side of the web-wall in a cross configuration (Fig. 4a, Fig. 5a and Fig. 5b). In addition, circular plastic connectors with diameter of 6 cm and length 8 cm were used to fix the mesh bands with a spacing of $30-40$ cm, in order to further improve the load transfer from the structure to the mesh (Fig. 4b). An additional fixation system was also used, consisting of L-steel profiles $50\text{X}50-5$ mm placed at each inner corner, which were connected by tie rods Φ 14 mm to U-steel profiles $80\text{X}25-5$ mm placed on the façades of the wing-walls (Fig. 5c). In total, five rows of U-steel profiles were set for each façade with distance in range $30-50$ cm; in this way, the influence area of each crack was guaranteed to be covered by two tie rods.

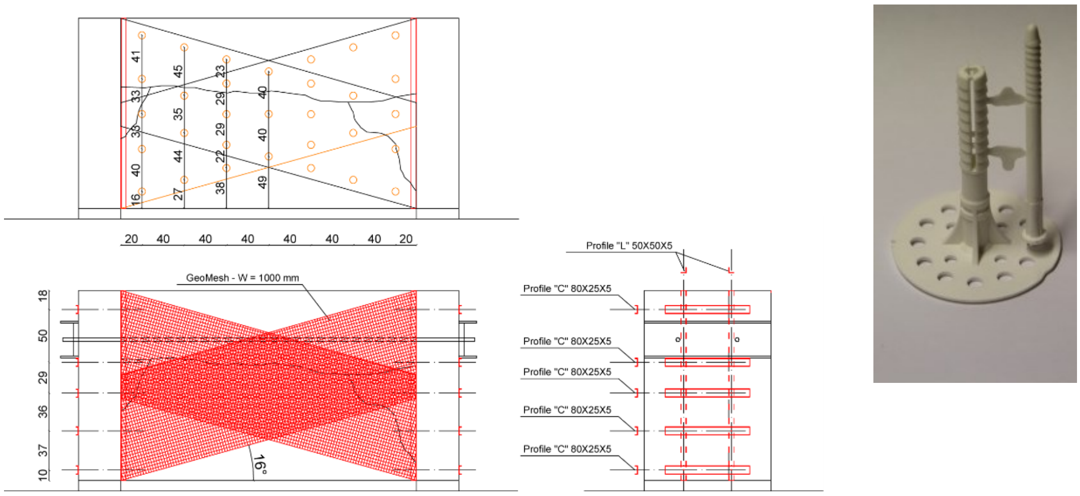

(a) (b)

Fig. 4 Proposed TRM strengthening solution: a) sScheme of TRM-strengthening and fixing system, and b) plastic connector.

(a) (b) (c)

Fig. 5 TRM strengthening of the GeoRE-IP model: a) web-wall prior the application of mortar, b) web-wall after the application of mortar and c) wing-wall.

2.2 Testing protocol

The cyclic tests were conducted by controlling the Displacement at the Control Point (d_{CP}), in the loading direction of a point at the top of the left wing, after a drying period of the strengthening of two months in laboratory conditions. The testing program considered cycle of increasing target displacements in both directions (positive and negative), and two repetitions for each step, as indicated in Fig. 6. Tab. 1 summarises the testing protocol, where d_{CP}^{peak} is the peak target displacement of the control point at each cycle, and the drift is the ratio between d_{CP}^{peak} and the elevation at which it is recorded. Additional dynamic identification tests by means of Operational Modal Analysis (OMA) were performed to detect natural frequencies (f) and mode shapes (Φ) of the wall and to track their change along the experimental program, which allowed to evaluate the evolution of damage [56][57][58][59]. Each dynamic identification test consisted of two setups of sixteen accelerometers (model PCB 393B12, 0.15 to 1000 Hz frequency range, 10000 mV/g sensitivity, 8μg resolution), of which two were fixed reference sensors (REF), to acquire the response over a grid with 4x5 points, while further four accelerometers were placed at the steel plate (G#), aiming at evaluating possible alterations in the boundary conditions of the wall along the tests. Additional scheme of the setup of the accelerometers can be found in Fig. 7 and in [41]. To guarantee the basic assumption of white noise and obtain accurate data resolution, the duration of each dynamic identification record was of 20 minutes with a sampling frequency of 200 Hz. The obtained signals, which were labelled as DI-GeoRE-IP-#*number of test*, were analysed with ARTeMIS Modal software [60]. The first dynamic identification test (DI-GeoRE-IP-01) was performed on the strengthened model before being tested; further dynamic identifications were performed after the fourth cycle (DI-GeoRE-02), after the sixth cycle (DI-GeoRE-IP-03) and at the end of the ninth cycle (DI-GeoRE-IP-04), as reported in Fig. 5 and Tab. 1. It is specified that the testing protocol was conducted in consecutive phases; therefore, the loading was interrupted and the actuator disconnected once that each cycle was completed. In this way, the effect of the actuator on the dynamic identification tests was null.

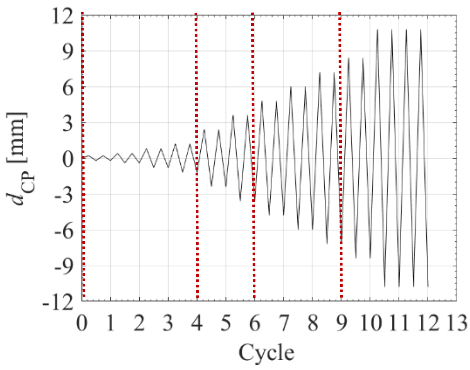

Fig. 6 Loading profile of the strengthened model GeoRE-IP and dynamic identification test DI-GeoRE-IP (dashed lines).

Tab. 1 Testing protocol of the strengthened model GeoRE-IP.

Cycle	Loading rate [μm/s]	d_{CP}^{peak} [mm]	Drift [%]
	DI-GeoRE-IP-01		
1	5	± 0.4	0.02
2	5	± 0.8	0.04
3	15	± 1.2	0.07
4	30	± 2.4	0.13
	DI-GeoRE-IP-02		
5	60	± 3.6	0.19
6	60	± 4.8	0.27
	DI-GeoRE-IP-03		
7	60	± 6.0	0.34

8	60	± 7.2	0.40
9	60	± 8.4	0.47
DI-GeoRE-IP-04			
10	60	± 10.8	0.61
11	60	± 10.8	0.61

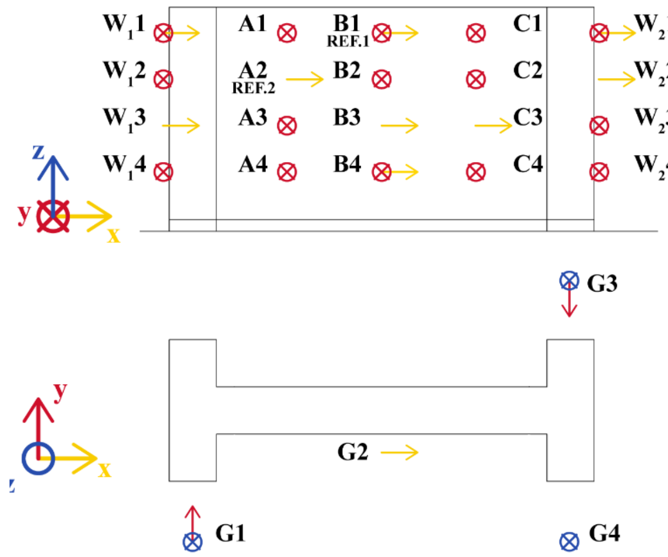

Fig. 7 Setup of accelerometers for dynamic identification tests.

The deformations during the tests were monitored by a set of four LVDTs placed at each wing-wall, which measured displacements in the loading direction along a vertical profile (LVDT-a1 to LVDT-d1, and LVDT-a5 to LVDT-d5). The relative displacements between the wing-walls and the web-wall were recorded by four LVDTs which were set horizontally at each inner corner (LVDT-a2 to LVDT-d2, and LVDT-a4 to LVDT-d4). To monitor the possible sliding at the foundation interface, additional three LVDTs were set at the base of the model (LVDT-g1, LVDT-g2 and LVDT-g3); while the deformations at the middle-third zone of the web-wall were recorded by six LVDTs placed in horizontal, vertical, and diagonal directions. Additional scheme of the setup of the LVDTs can be found in Fig. 8 and in [41].

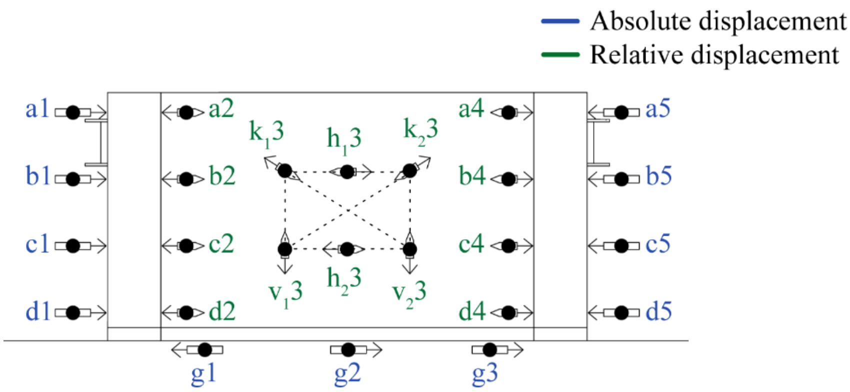

Fig. 8 Setup of LVDTs.

3 Strengthened model GeoRE-IP: results and discussion

The results of the in-plane cyclic test for the GeoTRM-strengthened Rammed Earth model GeoRE-IP are here discussed and compared with those of the unstrengthened model URE-IP, in terms of cracking pattern, dynamic properties, displacements, base shear coefficient, stiffness decay, energy-based analysis and proposal of bi-linear and linear equivalent systems.

3.1 Cracking pattern

The GeoRE-IP model showed at the third cycle minor cracks in correspondence of the main crack of the previous URE-IP model (Fig. 9). Afterwards, those cracks were progressively more evident and detachment of the mortar in the surrounding areas was observed. At the final stage, further diagonal cracks opened parallel to the diagonal cracks previously observed in URE-IP model (Fig. 9), while another horizontal crack formed at the top zone of the web-wall (Fig. 9a) which was not detected in the previous URE-IP model (Fig. 9b). Further cracks were found only in the GeoRE-IP at the wing-walls close to the steel profiles, yet along an interface between rammed earth layers (Fig. 9a). In addition, a crack at the base of the left wing-wall indicated a likely rocking mechanism in the GeoRE-IP mock-up (Fig. 9a). In general, the overall cracking pattern suggested that the damage state of the previous unstrengthened structure was difficult to recover from; nonetheless, the TRM strengthening was effectively able to redistribute the loads involving entirely the structure, as demonstrated by new cracks opened in different locations with respect to the URE-IP crack pattern (Fig. 8).

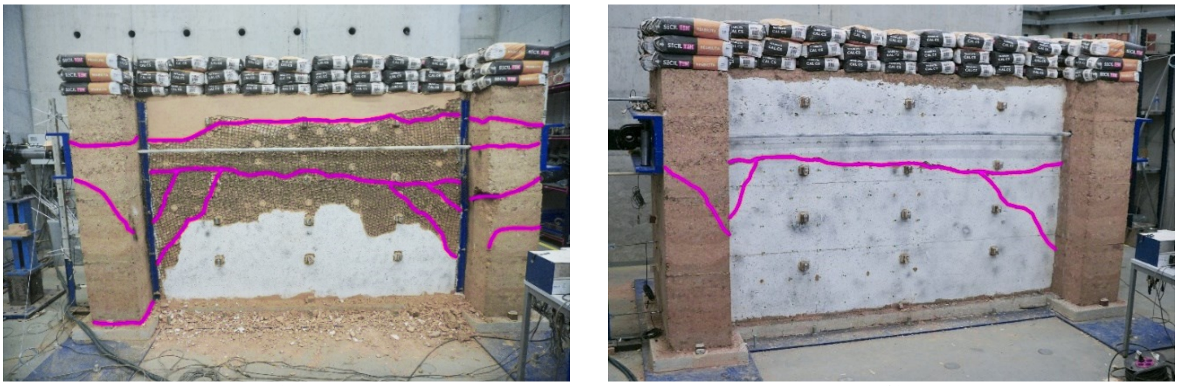

(a) (b)

Fig. 9 Cracking pattern of: a) GeoRE-IP model, and b) URE-IP model.

3.2 Dynamic properties

Five natural frequencies and corresponding mode shapes were distinguished in DI-GeoRE-IP-01. The first frequency is $f_1 = 17.06$ Hz and corresponds to an out-out-plane bending of the web-wall (Fig. 10a); the second frequency is $f_2 = 24.68$ Hz and involves the torsion of the model with its boundaries rotating out-of-plane in counterphase (Fig. 10b); the third frequency is $f_3 = 29.86$ Hz and corresponds to a combined movement of the in-plane and out-of-plane of the web-wall at the top (Fig. 10c); the fourth frequency is $f_4 = 33.20$ Hz and entails the out-of-plane movements of the boundaries in counterphase with the bending of the middle-section of the wall (Fig. 10d); the fifth frequency is $f_5 = 34.30$ Hz and corresponds to a mode shape similar to the third mode shape (Fig. 10e).

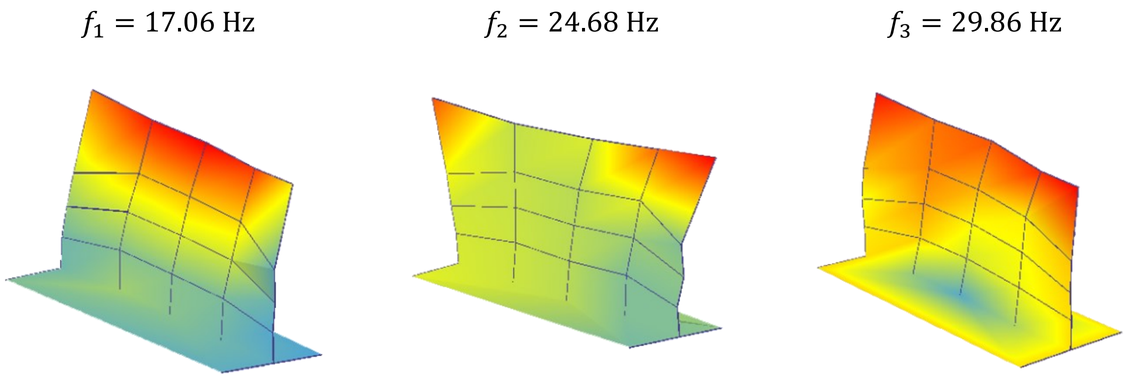

(a) (b) (c)

$f_4 = 33.20$ Hz $\quad$ $f_5 = 34.30$ Hz

(d) (e)

Fig. 10 Natural vibration modes of the strengthened model obtained from the DI-GeoRE-IP-01 test: a) Mode 1, b) Mode 2, c) Mode 3, d) Mode 4, and e) Mode 5.

To evaluate the influence of the TRM-strengthening on the dynamic properties of the damaged structure, a comparison between the eigenvalues of the first OMA of the strengthened wall (DI-GeoRE-IP-01) and the natural frequencies of the last OMA of the unstrengthened model (DI-URE-IP-03) was conducted. The Modal Assurance Criterion (MAC) of the respective OMA is illustrated in Fig. 11, in which the red shapes refer to DI-URE-IP-03 and the blue ones are DI-GeoRE-IP-01. The results in terms of natural frequencies of DI-URE-IP-03 and DI-GeoRE-IP-01, and variance of the eigenvalues evaluated as the percentage difference on the base of DI-URE-IP-03 are summarised in Tab. 2. It can be observed that the mode shapes related to the first frequency f_1, the third frequency f_3 and the fifth frequency f_5 of the DI-GeoRE-IP-01 paired with mode shapes of the ordered three frequencies of the DI-URE-IP-03, as MAC attained reliable values in the range 0.72 – 0.95. Consequently, the comparison of the natural frequencies indicated that the TRM-strengthening influenced the modal parameters of the damaged structure. In fact, the variance of the eigenvalues resulted null for f_1 and f_3; whereas a difference of 4% was attained in case of f_5. Nonetheless, it should be noted that, in case of DI-GeoRE-IP-01, mode shapes involving the out-of-plane of the core-wall were detected with the natural frequencies f_2 and f_4, while such mode shapes were not observed in DI-URE-IP-03 of the damaged structure.

Mode 1 **Mode 3** **Mode 5**

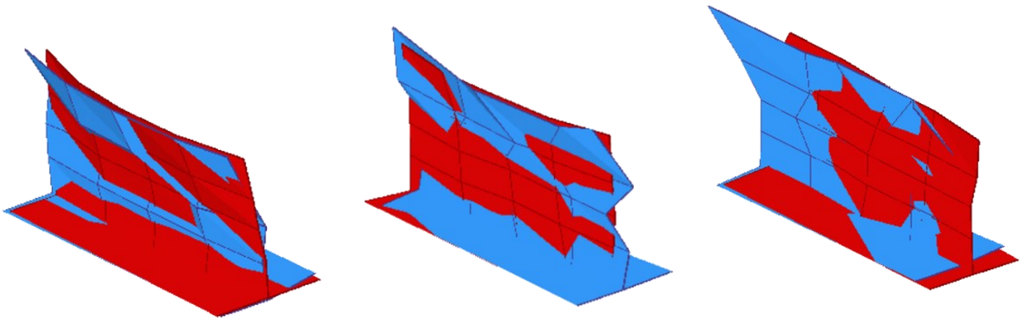

$MAC = 0.72$ $MAC = 0.95$ $MAC = 0.84$

Fig. 11 MAC between tests DI-URE-IP-03 and DI-GeoRE-IP-01.

Tab. 2 Comparison of results of natural frequencies between tests DI-URE-IP-03 and DI-GeoRE-IP-01.

	f_1 [Hz]	f_2 [Hz]	f_3 [Hz]	f_4 [Hz]	f_5 [Hz]
DI-URE-IP-03	17.08	-	29.92	-	32.80
DI-GeoRE-IP-01	17.06	24.68	29.86	33.20	34.30
Variation	0 %	-	0 %	-	4 %

The results of the entire sequence of dynamic identification tests on the GeoRE-IP model are reported in Fig. 12 and Tab. 3. In general, a decrease of the values of all the frequencies can be observed, which indicates likely damage in the structure. To quantify the level of damage, isotropic damage [61] between the eigenvalue i in the first dynamic identification and in the dynamic identification n can be assumed [62], while supposing that the seismic mass participating does not change significantly throughout the test. Considering the shape of the first mode and that the variation of the bending stiffness can be related to the variation of the thickness of the wall, the damage index results in a cubic correlation between the structural stiffness as in Eq. 1 [63]:

$$d_{\mathrm{i,n}} = 1 - \left(\frac{f_{\mathrm{i,n}}}{f_{\mathrm{i,0}}}\right)^6 \quad \text{(Eq. 1)}$$

where $f_{\mathrm{i,n}}$ represents the *i-th* natural frequency identified at the *n-th* dynamic identification test, and $f_{\mathrm{i,0}}$ is the *i-th* natural frequency identified at the first dynamic identification test. However, it must be attested that the considered frequencies refer to the same mode shapes. Therefore, the MAC of the modes being compared must be close to 1. The resulting MAC is reported in Tab. 3, which showed a general correspondence between the mode shapes of the first dynamic identification test (DI-GeoRE-

IP-01) and the other dynamic identification tests ($MAC > 0.80$), except for the mode shape associated to f_4 of DI-GeoRE-IP-04. Therefore, the damage indicator d (Eq. 1) was calculated for each frequency and reported in Fig. 13 as function of the cumulative displacement of the control point achieved at the time of the OMA (d_{cum}^{OMA}). At the last dynamic identification test, the damage index arose in the range 0.18 – 0.60, for the frequencies $f_1$and f_4 respectively. Although such level of damage is relevant for rammed earth structures, the TRM-strengthening could prevent instability and collapse of the model.

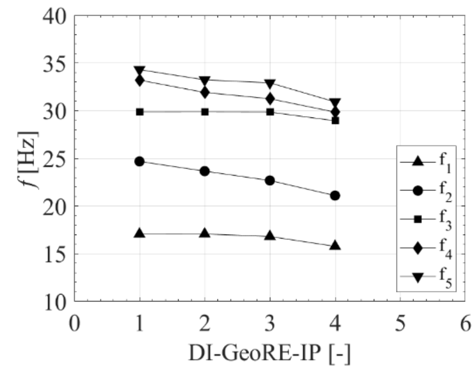

Fig. 12 Change in frequency values of the strengthened model GeoRE-IP.

Tab. 3 Natural frequencies detected for each dynamic identification DI-GeoRE-IP.

	f_1[Hz]	f_2[Hz]	f_3[Hz]	f_4[Hz]	f_5[Hz]
DI-GeoRE-IP-01	17.06	24.68	29.86	33.20	34.30
DI-GeoRE-IP-02	17.07 ($MAC = 0.97$)	23.66 ($MAC = 0.83$)	29.87 ($MAC = 0.97$)	31.91 ($MAC = 0.86$)	33.23 ($MAC = 0.91$)
DI-GeoRE-IP-03	16.81 ($MAC = 0.95$)	22.68 ($MAC = 0.82$)	29.85 ($MAC = 0.98$)	31.25 ($MAC = 0.91$)	32.92 ($MAC = 0.93$)
DI-GeoRE-IP-04	15.78 ($MAC = 0.94$)	21.10 ($MAC = 0.81$)	28.94 ($MAC = 0.94$)	29.85 ($MAC = 0.46$)	30.92 ($MAC = 0.87$)

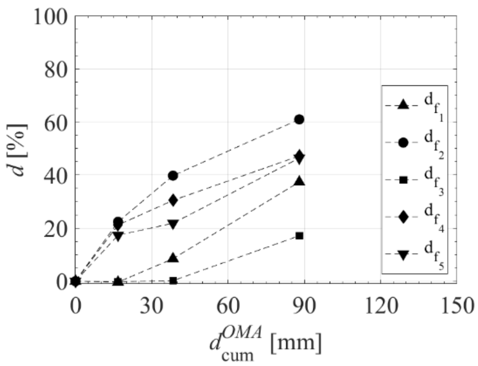

Fig. 13 Evolution of the damage indexes of the strengthened model GeoRE-IP.

3.3 Displacement profiles

The displacements achieved by the GeoRE-IP model are presented in Fig. 14, which considered the horizontal envelope profiles distinctly for both wing-walls and each direction. An almost linear envelope was observed up to the fourth cycle. Subsequently, the main horizontal crack in the web-wall re-opened and developed as a discontinuity, which was evident in the profiles of positive displacements (Fig. 14a and Fig. 14b). Subsequently, the difference in the displacements at different levels was pronounced with the increase of the target drift, suggesting the sliding of top block along the main horizontal crack. Nonetheless, such response was observed only for the positive envelopes (Fig. 14a and Fig. 14b), whereas linear profiles were detected for envelopes of negative displacements, as shown in Fig. 14c and Fig. 14d, which might be due to some asymmetry of the loading protocol (see Fig. 15). It should be noted that such asymmetry was caused by technical problems of the testing setup, in which the applied displacements in the negative direction were higher than those in the positive. Therefore, residual displacements in positive direction could be difficult to recover in the bottom part of the model.

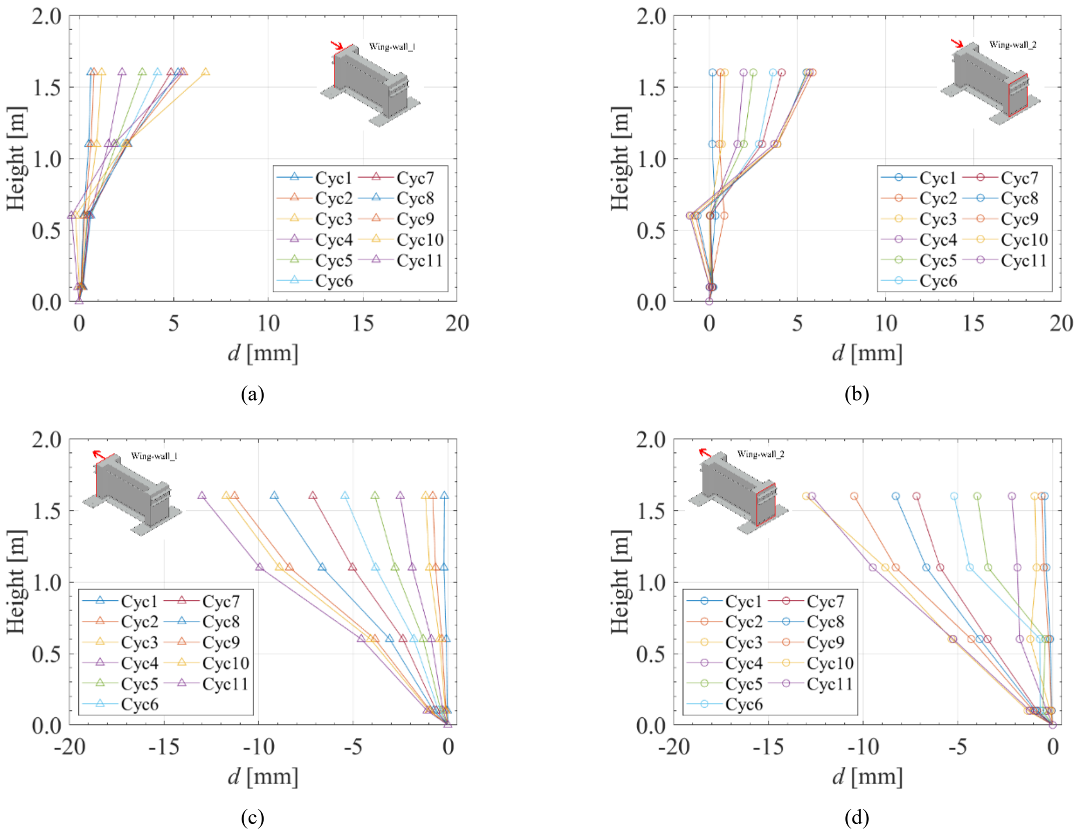

Fig. 14 Deformation profiles obtained for the strengthened model GeoRE-IP: a) positive horizontal displacement of the left wing, b) positive horizontal displacement of the right wing, c) negative horizontal displacement of the left wing, and c) negative horizontal displacement of the right wing.

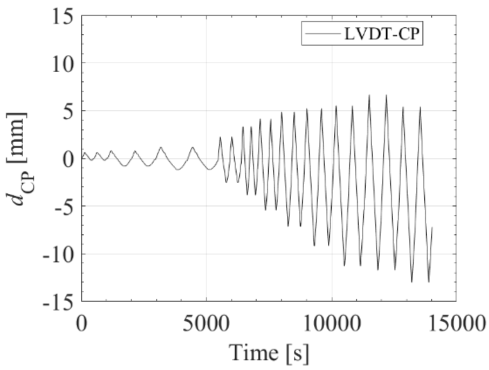

Fig. 15 Asymmetric loading profile of the strengthened model GeoRE-IP.

3.4 Base shear coefficient

The overall curves of the cyclic test are shown in Fig. 16a, considering the displacement of the control point (d_{CP}) and the related Base Shear Coefficient (BSC), which is calculated as the ratio between the Base Shear Force (BSF), assumed equal to the force measured by the actuator, and the self-weight of the wall. In addition, to analyse the different response of the model due to the repetition of the load path, the envelope of BSC peaks in both directions were considered for each loop separately in Fig. 16b, which resulted similar along the linear branch and part of the nonlinear behaviour. Afterwards, the BSC decreased from the first to the second loop in the same cycle, in particular when the maximum capacity was attained. Such difference between loops can be ascribed to the further damage induced to the structure and the TRM. It is noted that the response envelopes of both directions was similar up to the maximum positive BSC; subsequently, the in-plane shear capacity of the structure differed according to the loading direction due to the asymmetry of the loading profile applied (Fig. 16c).

The peak BSF towards the positive direction was 97.13 kN and was achieved for a displacement of 6.667 mm during the tenth cycle, to which corresponds a BSC of 1.23 and a drift of 0.42%. While the peak BSF towards the negative direction was 101.66 kN and was reached with a displacement of 9.148 mm, which is equivalent to a BSC of 1.29 and a drift of 0.57%, respectively.

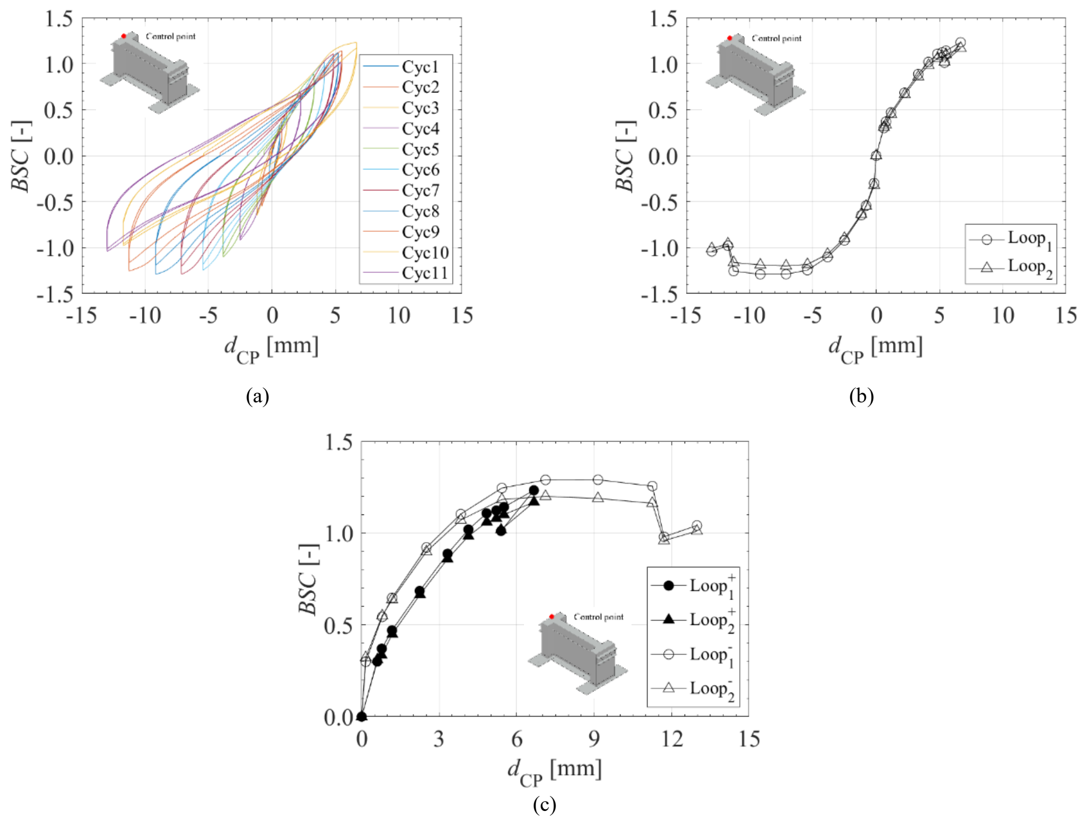

Fig. 16 Response curves of the GeoRE-IP model: a) all cycles, b) overall envelope for each loading loop, and c) comparison between the negative and positive loading directions.

To assess the effectiveness of the TRM-strengthening the envelope curves of GeoRE-IP were compared to URE-IP. The results showed that the strengthened rammed earth model was characterised by an early nonlinear response (Fig. 17), which confirmed that the previous damage state could not be recovered by the TRM-strengthening. Nonetheless, analysing the peak of BSC for loading in the positive direction, the GeoRE-IP presented a gain of 4% in shear strength capacity that was attained with a drift increase of 600%, with respect to the unstrengthened model URE-IP; whereas, in the case of the loading in the negative direction, the strengthened model could recover up to 93% of the BSC, however the peak BSC was achieved with an increment of 235% in drift (Tab. 4).

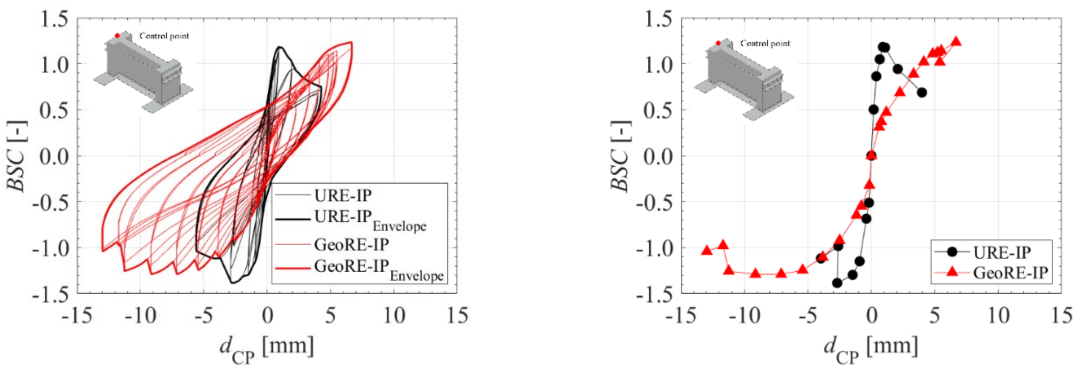

(a) (b)

Fig. 17 Comparison between the envelopes of the response curves of the unstrengthened and strengthened models: a) overall curves, and b) envelope of the cycles.

Tab. 4 Comparison of the main results of the unstrengthened and strengthened models.

Model	BSF^{+}_{peak} **[kN]**	BSC^{+}_{peak} **[-]**	$d^{+}_{BSF_{\text{peak}}}$ **[mm]**	**Drift [%]**	BSF^{-}_{peak} **[kN]**	BSC^{-}_{peak} **[-]**	$d^{-}_{BSF_{\text{peak}}}$ **[mm]**	**Drift [%]**
URE-IP	93.18	1.18	0.900	0.06	- 109.14	- 1.39	- 2.700	- 0.17
GeoRE-IP	97.13	1.23	6.667	0.42	- 101.66	- 1.29	- 9.148	- 0.57
GeoRE-IP/URE-IP	104 (%)	104 (%)	740 (%)	700 (%)	93 (%)	93 (%)	339 (%)	335 (%)

3.5 Stiffness degradation

Additional investigation on the deterioration due to cyclic loading was based on the evolution of the lateral stiffness. The lateral stiffness (K) was individuated for each loop and it was calculated by means of linear fitting of the BSF and the displacement of the control point according to different scenarios; in particular, the stiffness associated to the positive loading $\left(K_{\text{L}^{+}_{\text{Loop}}}\right)$ was evaluated in the range of 40% - 80% of the positive peak force; similarly, the stiffness associated to the negative loading $\left(K_{\text{L}^{-}_{\text{Loop}}}\right)$ considered the range 40% - 80% of the negative peak force. Whereas, the stiffness due to positive unloading $\left(K_{\text{UL}^{+}_{\text{Loop}}}\right)$ was calculated considering 70% of the force associated to the positive peak displacement as the upper boundary till the complete unload of the structure; in such a way, only the unloading due to the reverse displacement of the cycle was taken into account. The same was performed for the stiffness due to negative unloading $\left(K_{\text{UL}^{-}_{\text{Loop}}}\right)$, which was assessed in the range of

70% of the force associated to the negative peak displacement up to the complete unload of the structure. The values of stiffness were correlated with the cumulative displacement, calculated as the sum of the absolute values of displacement of the upper boundary of ranges up to that specific scenario, namely loading $\left(d_{\mathrm{cum}}^{K_{\mathrm{L}}}\right)$ and unloading $\left(\mathrm{d}_{\mathrm{cum}}^{\mathrm{K_{UL}}}\right)$ as in (Eq. 2) and in (Eq. 3).

$$d_{\mathrm{cum}}^{K_{\mathrm{L}}} = \sum \left| d_{80\%BSF_{\mathrm{peak}}} \right| \quad \text{(Eq. 2)}$$

$$d_{\mathrm{cum}}^{K_{\mathrm{UL}}} = \sum \left| d_{0\%post\_d_{\mathrm{peak}}} \right| \quad \text{(Eq. 3)}$$

The outcomes of the stiffness degradation of the strengthened model GeoRE-IP are presented in Fig. 18. Furthermore, Fig. 18 also compares the obtained results with those of the unstrengthened model URE-IP, in order to evaluate the influence of the TRM-strengthening on the damaged structure. As a result, a decreasing of the stiffness with the increasing of cumulative displacement was observed consequently to the development of cracks and the associated damage state. Nonetheless, the low value of the initial structural stiffness of GeoRE-IP and comparable measures of residual stiffness with URE-IP confirmed that the TRM-strengthening did not recover the previous original lateral stiffness of the structure, validating the observation of the dynamic identification tests.

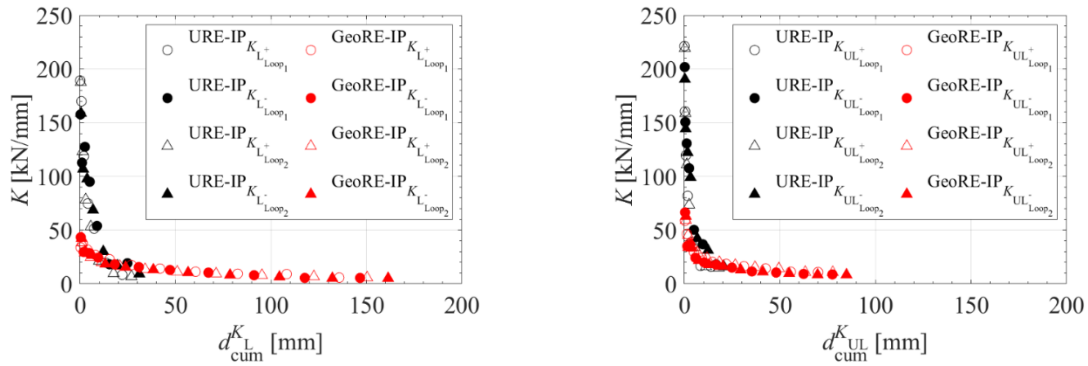

(a) (b)

Fig. 18 Stiffness degradation of the strengthened model GeoRE-IP and comparison with that of the un-strengthened one: a) loading stiffness, and b) unloading stiffness.

3.6 Energy-based analysis

The energy dissipated by the structure was analysed as function of the input energy of the system for each loop and for each cycle. The dissipated energy for a complete loop $\left(E_{\mathrm{dis}}^{\mathrm{Loop}}\right)$ was calculated as the integral of the BSF- d_{CP} curve along the entire loop (Eq. 4); while the input energy $\left(E_{\mathrm{sys}}^{\mathrm{Loop}}\right)$ was evaluated as the area of the BSF- d_{CP} curve along the single loading path, hence up to the positive peak displacement and the negative peak displacement (Eq. 5). From here, the dissipated energy $\left(E_{\mathrm{dis}}^{\mathrm{cyc}}\right)$ and the input energy $\left(E_{\mathrm{sys}}^{\mathrm{cyc}}\right)$ for each cycle is the sum of the corresponding components of the loops (Eq. 6)(Eq. 7); while the cumulative dissipated energy $\left(E_{\mathrm{dis}}^{\mathrm{cum}}\right)$ is the cumulative sum of the dissipated energy along the test and the cumulative input energy $\left(E_{\mathrm{sys}}^{\mathrm{cum}}\right)$ is the cumulative sum of the input energy along the test (Eq. 8) and (Eq. 9).

$$E_{\mathrm{dis}}^{\mathrm{Loop}} = \oint_{\mathrm{i=1:2}}^{\mathrm{Loop}} F dD \qquad \text{(Eq. 4)}$$

$$E_{\mathrm{sys}}^{\mathrm{Loop}} = \int_0^{D_{\mathrm{peak}}^{+}} F dD + \int_0^{D_{\mathrm{peak}}^{-}} F dD \qquad \text{(Eq. 5)}$$

$$E_{\mathrm{dis}}^{\mathrm{cyc}} = E_{\mathrm{dis}}^{\mathrm{Loop_1}} + E_{\mathrm{dis}}^{\mathrm{Loop_2}} \qquad \text{(Eq. 6)}$$

$$E_{\mathrm{sys}}^{\mathrm{cyc}} = E_{\mathrm{sys}}^{\mathrm{Loop_1}} + E_{\mathrm{sys}}^{\mathrm{Loop_2}} \qquad \text{(Eq. 7)}$$

$$E_{\mathrm{dis}}^{\mathrm{cum}} = \sum_{\mathrm{n}}^{\mathrm{cycle}} E_{\mathrm{dis}}^{\mathrm{cyc}} \qquad \text{(Eq. 8)}$$

$$E_{\mathrm{sys}}^{\mathrm{cum}} = \sum_{\mathrm{n}}^{\mathrm{cycle}} E_{\mathrm{sys}}^{\mathrm{cyc}} \qquad \text{(Eq. 9)}$$

As can be observed in Fig. 19, a linear correlation is found between the input and the dissipated energy, in spite of considering loops, cycles or cumulative energy; while a ratio of dissipated energy to input energy was found to be in a range of 57% - 64%. In addition, a slight difference is observed when the dissipated energy of two consecutive loops is compared, although the structure was led to plastic domain suggesting that the ductile capacity of the TRM-strengthening was not compromised. The energy dissipation of the GeoRE-IP model was also analysed in comparison with that of the URE-IP model. It is noted that, although the TRM-strengthening could not recover the existing damage in the structure, it is able to provide the dissipative capacity of the original system. Indeed, for the same input energy, the GeoRE-IP model dissipated similar amount of energy as that of the URE-IP model.

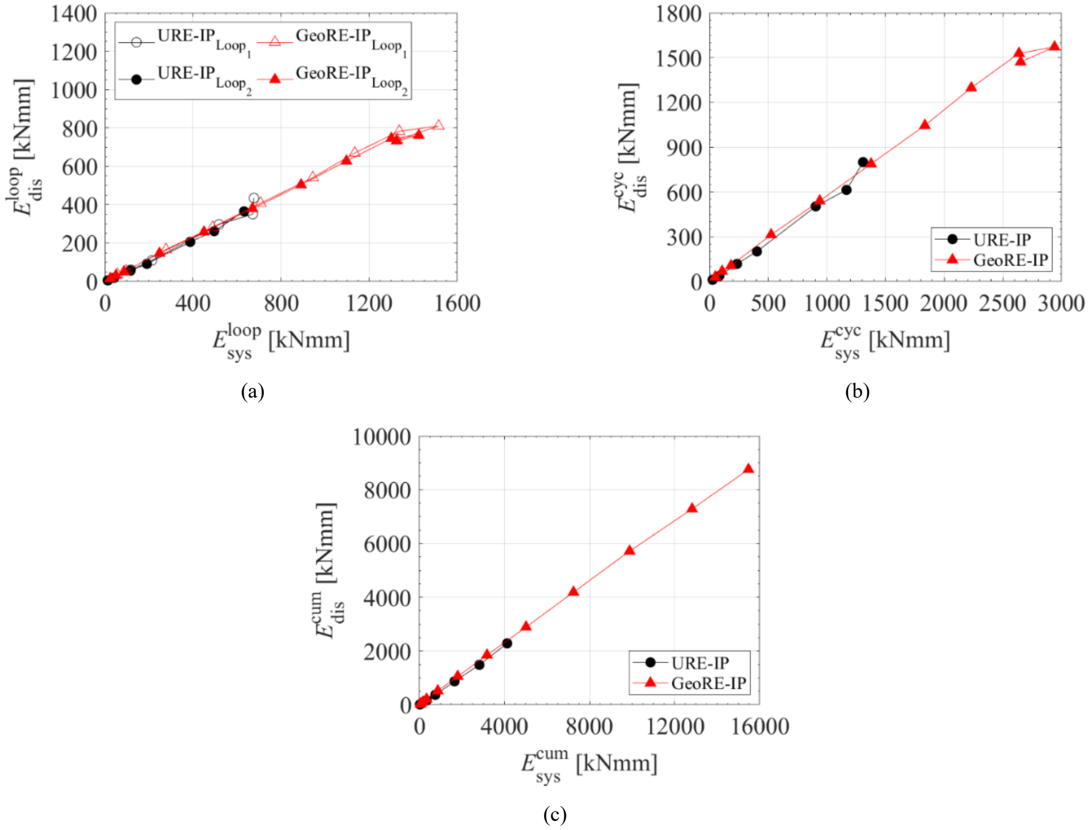

Fig. 19 Dissipated and input energy of the strengthened model GeoRE-IP and comparison with that of the un-strengthened one: a) loops, b) cycles, and c) cumulative energy.

Subsequently, the equivalent damping coefficient was evaluated as:

$$\xi_{\mathrm{eq}} = \frac{E_{\mathrm{dis}}^{\mathrm{Loop}}}{2\pi E_{\mathrm{sys}}^{\mathrm{Loop}}} \qquad \text{(Eq. 10)}$$

The equivalent damping coefficient (ξ_{eq}) is reported in Fig. 20 as a function of the input energy, which resulted almost constant throughout the test with a value of approximately 9%. Such result might be a consequence of the non-linear behaviour of the structure that occurred already at early cycles.

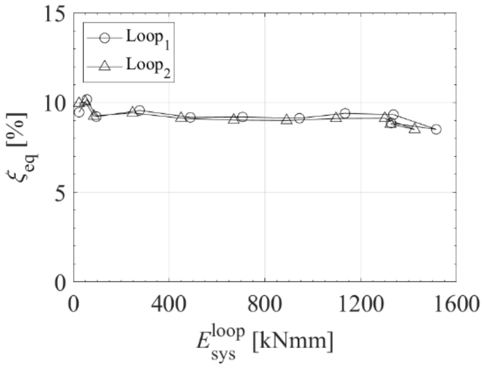

Fig. 20 GeoRE-IP equivalent damping coefficient for each loop.

3.7 Bi-linear and linear equivalent systems

As the rammed earth wall dissipated hysteretic energy, an equivalent elastic-perfectly plastic system was idealised to simplify the non-linear behaviour following the indications given in [42][43][44][45]. Accordingly, the ultimate displacement (d_{u}) of the bi-linear curve was individuated at a decrease of 15% of BSF_{peak} of the experimental curve and the secant stiffness (K) of the equivalent system was constrained to the 60% of BSF_{peak} of the original curve. Therefore, the yielding force (F_{y}) and displacement (d_{y}) of the equivalent system were calculated balancing the energy of the experimental envelope curve and the energy of the idealised bi-linear curve. In addition, to further represent the experimental nonlinear response with an equivalent linear elastic structure, the elastic strength (F_{e}) was defined by the equivalence of the energy subtended the linear curve and the bi-linear curve and assuming the same stiffness (K). Subsequently, the ductility factor (μ), the behaviour factor (q) and the reserve strength ratio, or overstrength, (γ) were calculated, as in (Eq. 11), (Eq. 12), and (Eq. 13), and as indicated in [41][42][43][44][45].

$$\mu = \frac{d_{\mathrm{u}}}{d_{\mathrm{y}}} \qquad \text{(Eq. 11)}$$

$$q = \frac{F_{\mathrm{e}}}{F_{\mathrm{y}}} \qquad \text{(Eq. 12)}$$

$$\gamma = \frac{F_{\mathrm{peak}}}{F_{\mathrm{y}}} \qquad \text{(Eq. 13)}$$

Subsequently, the equivalent elastic and elastic-perfectly plastic systems of the GeoRE-IP model were compared with the corresponding URE-IP systems (see Tab. 5 and Fig. 21). With regard to the positive loading direction, it should be noted that the experimental curve did not achieve softening post peak due to the aforementioned problems in the testing protocol. As a consequence, since the equivalent bi-linear and linear system could not consider the actual ductile capacity of the structure, the equivalent systems for the positive loading direction are not here discussed. The GeoRE-IP model yielding force (F_y) and the elastic force (F_e) are comparable to the corresponding values of the URE-IP model, whereas the yielding displacement (d_y) of the equivalent GeoRE-IP system is about 323% higher than the value of URE-IP case. As consequence, the equivalent structural stiffness (K) of the TRM-strengthened model is about 29% of the original URE-IP model, which reflects the experimental outcome. In addition, the equivalent ultimate displacement (d_u) of the GeoRE-IP model increased about 339%, highlighting the deformation capacity introduced by the TRM-strengthening, but also influenced by its lower lateral stiffness. Nonetheless, the overall ductility (μ) and behaviour factor (q) of the GeoRE-IP model improved about 5% and 3%, respectively, compared to the original structure; while the overstrength (γ) can be assumed equal.

Tab. 5 Comparison of parameters of the equivalent elastic-perfectly plastic and elastic systems for the un-strengthened model URE-IP and the strengthened model GeoRE-IP.

Negative displacement	F_y **[kN]**	d_y **[mm]**	K **[kN/mm]**	d_u **[mm]**	F_e **[kN]**	μ **[-]**	q **[-]**	γ **[-]**
URE-IP	102.83	0.888	115.84	3.698	278.45	4.17	2.71	1.06
GeoRE-IP	97.49	2.865	34.03	12.533	271.40	4.37	2.78	1.04
URE-IP/GeoRE-IP	95 (%)	323 (%)	29 (%)	339 (%)	97 (%)	105 (%)	103 (%)	98 (%)

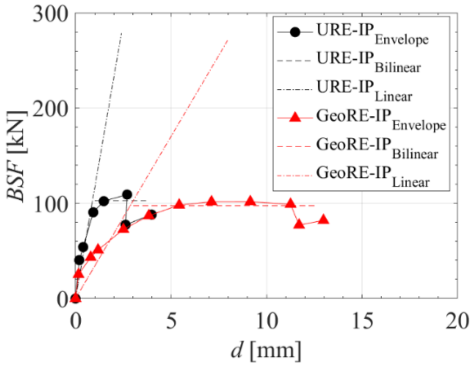

Fig. 21 Comparison of the equivalent elastic-perfectly plastic and elastic systems of the URE-IP and GeoRE-IP models for loading in the negative direction.

4 Conclusions

The experimental program discussed in this paper intended to evaluate the effectiveness of a TRM-strengthening solution compatible with rammed earth, by comparing the outcomes of the unstrengthened model (URE-IP) with those of the damaged model after being strengthened (GeoRE-IP). The cracking pattern of the GeoRE-IP model indicated that, although the previous damage could not be recovered, the TRM-strengthening was able to redistribute the loads involving entirely the structure. The fact that the previous damage state was not recovered was demonstrated, as well, by comparing the dynamic properties of the GeoRE-IP model with those of the URE-IP model. The natural frequencies and mode shapes of the model prior and subsequently to the application of the TRM-strengthening were similar. Such result was also demonstrated by analysing the degradation of the structural stiffness of the GeoRE-IP model, which at early levels of loading showed values comparable to those assessed for the damaged URE-IP model. A degradation of force due to the repetition of loads in the GeoRE-IP model was observed through the comparison of the envelopes of the BSF- d_{CP} curves of each loop. Despite the GeoRE-IP model showed an early nonlinear response consequent to the former damage state of the model, the TRM-strengthening resulted effective as it allowed achieving up to 104% of the BSC of the original structure for a drift increase of 600%. Therefore, the effectiveness of the TRM-strengthening was found in the enhanced dissipative capacity of the GeoRE-IP model compared to the URE-IP one, as proved by the energy dissipation in respect to the demanded energy. Similar findings were obtained in the proposed equivalent elastic and elastic-perfectly plastic systems. Indeed, the yielding and the ultimate displacements of GeoRE-IP model were, respectively, 323% and 339% higher than those of the unstrengthened model; while the ductility and behaviour factor of the strengthened model were improved by about 5% and 3% with respect of the original structure. In conclusion, the TRM-strengthening solution adopted was effective in recovering the strength capacity of the original structure while providing further dissipative and ductility capacity. Nonetheless, the overall lateral stiffness was not recovered by the strengthening technique employed, for which other repairing interventions might be required. Anyway, from the authors' experience, the full recovery of initial lateral stiffness is hardly possible in these cases.

5 Acknowledgments

This work was partly financed by FEDER funds through the Operational Programme Competitiveness Factors (COMPETE 2020) and by national funds through the Foundation for Science and Technology (FCT) within the scope of project SafEarth - PTDC/ECM-EST/2777/2014 (POCI-01-0145-FEDER-016737). The support from grants SFRH/BD/131006/2017 and SFRH/BPD/97082/2013 is also acknowledged. Acknowledgments are addressed to the Laboratory of Structures (LEST) of the University of Minho and to João Bernardino, Lda. and TERRACRUA - Construções Ecológicas Unipessoal, Lda for building the rammed earth model.

6 Author contributions

Romanazzi A. – Conceptualization, methodology, acquisition of data, data analysis, formal analysis, investigation, writing original draft, review and editing, visualization.

Oliveira D.V. – Conceptualization, methodology, review, supervision, funding acquisition

Silva R.A. – Conceptualization, methodology, review, supervision, funding acquisition

Barontini A. – Acquisition of data, investigation, writing review and editing.

7 References

[1] Jaquin, P. A., Augarde, C. E., and Gerrard, C. M. (2008). Chronological description of the spatial development of rammed Earth techniques. International Journal of Architectural Heritage, 2(4), 377–400. https://doi.org/10.1080/15583050801958826

[2] Pacheco-Torgal, F., and Jalali, S. (2012). Earth construction: Lessons from the past for future eco-efficient construction. Construction and Building Materials, 29, 512–519. https://doi.org/10.1016/j.conbuildmat.2011.10.054

[3] Correia, M., Varum, H., and Lourenço, P. B. (2015). Common damages and recommendations for the seismic retrofitting of vernacular dwellings. In M. R. Correia, P. B. Lourenço, and H.

Varum (Eds.), Seismic Retrofitting: Learning from Vernacular Architecture (p. 241). Taylor and Francis Group, London.

[4] Lacoutre, L. E. Y., Bernal, P. C., Ortiz, J. C. R., and Valencia, D. R. (2007). Estudios de vulnerabilidad sísmica, rehabilitación y refuerzo de casas en adobe y tapia pisada. Apuntes: Revista de Estudios Sobre Patrimonio Cultural, 20(2), 286–303.

[5] Lourenço, P. B., Torrealva, D., Cancino, C., Wong, K., Karanikoloudis, G., and Ciocci, M. P. (2017). Innovative traditional technologies for rehabilitation and protection of earthen structures: the Getty conservation institute seismic retrofitting project. Proceeding of the 3rd International Conference on Protection of Historical Constructions, Lisbon, 12th - 15th July, May 2015, 12–15.

[6] Romanazzi, A., Oliveira, D.V., Silva, R.A., Candeias, P.X., Costa, A.C., and Carvalho, A. (2022) Out-of-plane shake table test of a rammed earth sub-assembly. Bull Earthquake Eng 20, 8325–8356. https://doi.org/10.1007/s10518-022-01525-6

[7] Bui, T. T., Bui, Q. B., Limam, A., and Maximilien, S. (2014). Failure of rammed earth walls: From observations to quantifications. Construction and Building Materials, 51, 295–302. https://doi.org/10.1016/j.conbuildmat.2013.10.053

[8] Liu, K., Wang, M., and Wang, Y. (2015). Seismic retrofitting of rural rammed earth buildings using externally bonded fibers. Construction and Building Materials, 100(December), 91–101. https://doi.org/10.1016/j.conbuildmat.2015.09.048

[9] Lima, A., Viana, D., Gomes, F., Carlos, G. D., Sousa, G., Vasconcelos, G., Rodrigues, H., Varum, H., Ortega, J., Correia, M. R., Lourenço, P. B., and Barros, R. (2015). Local seismic culture in Portugal (Cultura sísmica local em Portugal) (M. R. Correia and G. D. Carlos, Eds.). Argumentum, Lisbon.

[10] Canivell, J. (2012). Characterization methodology to efficiently manage the conservation of historical rammed-earth buildings. In C. Mileto, F. Vegas, and CristiniV. (Eds.), Rammed Earth

Conservation (pp. 283–288). Taylor and Francis Group, London. https://doi.org/10.1201/b15164-51

[11] Van Balen, K., Papayianni, I., van Hees, R., Binda, L., and Waldum, A. (2005). Introduction to requirements for and functions and properties of repair mortars. Materials and Structures/Materiaux et Constructions, 38(282), 781–785. https://doi.org/10.1617/14319

[12] Bui, Q. B., Hans, S., Morel, J. C., and Do, A. P. (2011). First exploratory study on dynamic characteristics of rammed earth buildings. Engineering Structures, 33(12), 3690–3695. https://doi.org/10.1016/j.engstruct.2011.08.004

[13] Yamin, L. E., Phillips, C. A., Reyes, J. C., and Ruiz, D. M. (2004). Seismic behavior and rehabilitation alternatives for adobe and rammed earth buildings. Proceeding of the 13th World Conference on Earthquake Engineering, Vancouver, 1st - 6th August.

[14] Reyes, J. C., Rincon, R., Yamin, L. E., Correal, J. F., Martinez, J. G., Sandoval, J. D., Gonzalez, C. D., and Angel, C. C. (2020). Seismic retrofitting of existing earthen structures using steel plates. Construction and Building Materials, 230, 117039. https://doi.org/10.1016/j.conbuildmat.2019.117039

[15] Reyes, J. C., Smith-Pardo, J. P., Yamin, L. E., Galvis, F. A., Sandoval, J. D., Gonzalez, C. D., and Correal, J. F. (2019). In-plane seismic behavior of full-scale earthen walls with openings

retrofitted with timber elements and vertical tensors. Bulletin of Earthquake Engineering, 17(7), 4193–4215. https://doi.org/10.1007/s10518-019-00601-8

[16] Ramírez Eudave, R., Silva, R.A., Pereira, E., and Romanazzi, A. (2022) Early-age shrinkage and bond of LC-TRM strengthening in rammed earth. Construction and Building Materials, 350. https://doi.org/10.1016/j.conbuildmat.2022.128809

[17] Romanazzi, A., Oliveira, D.V., and Silva, R.A. (2021) An analytical bond stress-slip model for a TRM composite compatible with rammed earth. Construction and Building Materials, 310. https://doi.org/10.1016/j.conbuildmat.2021.125228

[18] Romanazzi, A., Oliveira, D.V., and Silva, R.A. (2018) Experimental investigation on the bond behavior of a compatible TRM-based solution for rammed earth heritage. International Journal of Architectural Heritage, 13, 7. https://doi.org/10.1080/15583058.2019.1619881

[19] De Felice, G., de Santis, S., Garmendia, L., Ghiassi, B., Larrinaga, P., Lourenço, P. B., Oliveira, D. v., Paolacci, F., and Papanicolaou, C. G. (2014). Mortar-based systems for externally bonded strengthening of masonry. Materials and Structures, 47(12), 2021–2037. https://doi.org/10.1617/s11527-014-0360-1

[20] Ghiassi, B., Marcari, G., Oliveira, D. v., and Lourenço, P. B. (2012). Numerical analysis of bond behavior between masonry bricks and composite materials. Engineering Structures, 43, 210–220. https://doi.org/10.1016/j.engstruct.2012.05.022

[21] Vargas, J. N. (1983). Earthquakes and adobe structures. Adobe: International Symposium and Training Workshop on the Conservation of Adobe. Final Report and Major Papers, Lima - Cusco, 10th - 22nd September.

[22] Vargas, J. N., Bariola, J., Blondet, M., and Mehta, P. K. (1986). Seismic strength of adobe masonry. Materials and Structures, 19(4), 253–258. https://doi.org/10.1007/BF02472107

[23] Vargas, J. N., Blondet, M., Ginocchio, F., and Garcia, G. (2005). 35 Años de investigaciones en sismo adobe: la tierra armada. Proceeding of International Conference SismoAdobe:

Architecture, Construction and Conservation of Earthen Buildings in Seismic Areas, Lima, 16th - 19th May.

[24] Vargas, J. N., Blondet Saavedra, M., and Torrealva Dávila, D. (2007). Construcción de casas saludables y sismoresistentes de adobe reforzado con geomallas: zona de la costa. Pontificia Universidad Católica del Perú. Fondo Editorial.

[25] Blondet, M., Torrealva, D., Garcia, G. V., Ginocchio, F., and Madueño, I. (2005). Using industrial materials for the construction of safe adobe houses in seismic areas. Proceedings of Earthbuild International Conference, Sydney, 19th - 21st January, 76–90.

[26] Michiels, T. L. G. (2015). Seismic Retrofitting Techniques for Historic Adobe Buildings. International Journal of Architectural Heritage, 9(8), 1059–1068. https://doi.org/10.1080/15583058.2014.924604

[27] Noguez, R., and Navarro, S. (2005). Reparacion de muros de adobe com el uso de mallas sinteticas. Proceeding of International Conference SismoAdobe: Architecture, Construction and Conservation of Earthen Buildings in Seismic Areas, Lima, 16th - 19th May.

[28] Zavala, C., and Igarashi, L. (2005). Propuesta de reforzamiento para muros de adobe. Proceeding of International Conference SismoAdobe: Architecture, Construction and Conservation of Earthen Buildings in Seismic Areas, Lima, 16th - 19th May.

[29] Figueiredo, A., Varum, H., Costa, A., Silveira, D., and Oliveira, C. (2013). Seismic retrofitting solution of an adobe masonry wall. Materials and Structures, 46(1–2), 203–219. https://doi.org/10.1617/s11527-012-9895-1

[30] Torrealva, D. (2016). Static and dynamic testing for validating the polymer grid as external reinforcement in earthen buildings. Brick and Block Masonry: Trends, Innovations and

Challenges - Proceedings of the 16th International Brick and Block Masonry Conference, IBMAC 2016, 873–882. https://doi.org/10.1201/b21889-109

[31] Torrealva, D., and Acero, J. (2005). Refuerzo sísmico de vivienda de adobe con malla exterior compatible. Memorias Del Seminario Internacional de Arquitectura, Construcción y Conservación de Edificaciones En Tierra En Áreas Sísmicas, SismoAdobe2005, PUCP.

[32] Blondet, M., Torrealva, D., Vargas, J. N., Velasquez, J., and Tarque, N. (2006). Seismic reinforcement of adobe houses using external polymer mesh. Proceeding of First European Conference on Earthquake Engineering and Seismology, Geneva, 3rd - 8th September.

[33] Bossio, S., Blondet, M., and Rihal, S. (2013). Seismic behavior and shaking direction influence on adobe wall structures reinforced with geogrid. Earthquake Spectra, 29(1), 59–84. https://doi.org/10.1193/1.4000096

[34] Reyes, J. C., Smith-Pardo, J. P., Yamin, L. E., Galvis, F. A., Angel, C. C., Sandoval, J. D., and Gonzalez, C. D. (2019). Seismic experimental assessment of steel and synthetic meshes for retrofitting heritage earthen structures. Engineering Structures, 198, 109477. https://doi.org/10.1016/j.engstruct

[35] Fagone, M., Kloft, H., Loccarini, F., and Ranocchiai, G. (2019). Jute fabric as a reinforcement for rammed earth structures. Composites Part B: Engineering, 175(June), 107064. https://doi.org/10.1016/j.compositesb.2019.107064

[36] Fagone, M., Loccarini, F., and Ranocchiai, G. (2017). Strength evaluation of jute fabric for the reinforcement of rammed earth structures. Composites Part B: Engineering, 113, 1–13. https://doi.org/10.1016/j.compositesb.2016.12.054

[37] Romanazzi, A., Van Gorp, M., Oliveira, D. v., Silva, R. A., and Verstrynge, E. (2019). Experimental shear behaviour of rammed earth strengthened with a TRM-based compatible

technique. Key Engineering Materials, 817 KEM, 544–551. https://doi.org/10.4028/www.scientific.net/KEM.817.544

[38] Wang, Y., Wang, M., Liu, K., Pan, W., and Yang, X. (2016). Shaking table tests on seismic retrofitting of rammed-earth structures. Bulletin of Earthquake Engineering, 15(3), 1037–1055. https://doi.org/10.1007/s10518-016-9996-2

[39] Miccoli, L., Müller, U., and Pospíšil, S. (2017). Rammed earth walls strengthened with polyester fabric strips: Experimental analysis under in-plane cyclic loading. Construction and Building Materials, 149, 29–36. https://doi.org/10.1016/j.conbuildmat.2017.05.115

[40] Wang, Y., Wang, M., and Liu, K. (2019). Experimental study of the Seismic Performance of Different Earth Walls and Their Seismic Retrofitting with Externally Bonded Fibers. Journal of Earthquake Engineering, 1–23. https://doi.org/10.1080/13632469.2019.1688206

[41] Romanazzi, A., Oliveira, D.V., Silva, R.A., Barontini, A., and Mendes, N. (2021) Performance of rammed earth subjected to in-plane cyclic displacement. Materials and Structures, 55, 2. https://doi.org/10.1617/s11527-022-01894-z

[42] BS EN 1998-1. (2004). Eurocode 8: Design of structures for earthquake resistance - Part 1 : General rules, seismic actions and rules for buildings. European Committee for Standardization.

[43] Consiglio Superirore dei Lavori Pubblici. (2008). Nuove norme techniche per le costruzioni, D.M. Infrastrutture 14/01/2008.

[44] Tomaževič, M. (1997). Seismic design of masonry structures. Progress in Structural Engineering and Materials, 1(1), 88–95. https://doi.org/10.1111/j.1749-6632.1989.tb22578.x

[45] Tomaževič, M. (2006). Earthquake resistant design of masonry buildings. In Series on Innovation in Structures and Construction - Vol. 1 (Vol. 1). Imperial College Press. https://doi.org/10.1007/978-3-319-76855-7_12

[46] LNEC E197. 1966. Solos. Ensaio de compactação. Lisboa: Laboratiorio Nacional de Engenharia Civil.

[47] Vasconcelos, R. (1993). Contribuição à aplicação de técnicas de inteligência artificial na tecnologia da fiação. PhD Thesis, Universidade Do Minho.

[48] ISO 3374. (2000). Reinforcement products. Mats and fabrics. Determination of mass per unit area. International Organization for Standardization.

[49] NATIONAL RESEARCH COUNCIL. (2004). Guide for the design and construction of externally bonded FRP systems for strengthening existing structures. In ACI committee 440 (p. 144).

[50] ASTM D6637. (2010). Standard Test Method for Determining Tensile Properties of Geogrids by the Single or. American Society for Testing and Materials. https://doi.org/10.1520/D6637-11.2

[51] de Felice, G., Aiello, M. A., Caggegi, C., Ceroni, F., de Santis, S., Garbin, E., Gattesco, N., Hojdys, Ł., Krajewski, P., Kwiecień, A., Leone, M., Lignola, G. P., Mazzotti, C., Oliveira, D. v., Papanicolaou, C., Poggi, C., Triantafillou, T., Valluzzi, M. R., and Viskovic, A. (2018). Recommendation of RILEM Technical Committee 250-CSM: Test method for Textile

Reinforced Mortar to substrate bond characterization. Materials and Structures/Materiaux et Constructions, 51(4), 1–9. https://doi.org/10.1617/s11527-018-1216-x

[52] BS EN 1015-3. (1993). Methods of test for mortar for masonry. Part 3: Determination of consistence of fresh mortar (by flow table). British Standards Institution.

[53] Gomes, M. I., Diaz Gonçalves, T., and Faria, P. (2019). The compatibility of earth-based repair mortars with rammed earth substrates. Proceeding of the 3rd Historic Mortars Conference, Glasgow, 11th - 14th September, 305–318. https://doi.org/10.1007/978-3-319-91606-4_22

[54] BS EN 1015-11. (1993). Methods of test for mortar for masonry. Part 11: Determination of flexural and compressive strength of hardened mortar. British Standards Institution.

[55] Gomes, M. I. (2013). Conservation of rammed earth construction: repairing mortars. PhD Thesis, Universidade Nova de Lisboa.

[56] Brownjohn, J. M. W., de Stefano, A., Xu, Y. L., Wenzel, H., and Aktan, A. E. (2011). Vibration-based monitoring of civil infrastructure: Challenges and successes. Journal of Civil Structural Health Monitoring, 1(3–4), 79–95. https://doi.org/10.1007/s13349-011-0009-5

[57] Das, S., Saha, P., and Patro, S. K. (2016). Vibration-based damage detection techniques used for health monitoring of structures: a review. Journal of Civil Structural Health Monitoring, 6(3), 477–507. https://doi.org/10.1007/s13349-016-0168-5

[58] Pepi, C., Cavalagli, N., Gusella, V., and Gioffrè, M. (2021). Damage detection via modal analysis of masonry structures using shaking table tests. Earthquake Engineering and Structural Dynamics, 50(8), 2077–2097. https://doi.org/10.1002/eqe.3431

[59] Ren, W.-X., and de Roeck, G. (2002). Structural Damage Identification using Modal Data. II: Test Verification. Journal of Structural Engineering, 128(1), 96–104. https://doi.org/10.1061/(asce)0733-9445(2002)128:1(96)

[60] ARTeMIS. (2013). Ambient response testing and modal identification software. SVS – Structural Vibration Solutions A/S. Modal 2.5. Denmark.

[61] Lemaitre, J., and Desmorat, R. (2005). Engineering damage mechanics: ductile, creep, fatigue and brittle failures. Springer Berlin Heidelberg. https://books.google.pt/books?id=WgeaXK6-ZgwC

[62] Candeias, P. (2008). Avaliação da vulnerabilidade sísmica de edifícios de alvenaria. (Seismic vulnerability assessment of ancient buildings). PhD Thesis, Universidade Do Minho.

[63] Giordano, E., Mendes, N., Masciotta, M. G., Clementi, F., Sadeghi, N. H., Silva, R. A., and Oliveira, D. v. (2020). Expeditious damage index for arched structures based on dynamic identification testing. Construction and Building Materials, 265, 120236. https://doi.org/10.1016/j.conbuildmat.2020.120236